

THE COOL SURGE FOLLOWING FLUX EMERGENCE IN A RADIATION-MHD EXPERIMENT

D. NÓBREGA-SIVERIO^{1,2}, F. MORENO-INSERTIS^{1,2}, AND J. MARTÍNEZ-SYKORA^{3,4}

¹ Instituto de Astrofísica de Canarias, Via Lactea, s/n, E-38205 La Laguna (Tenerife), Spain
² Department of Astrophysics, Universidad de La Laguna, E-38200 La Laguna (Tenerife), Spain

³ Lockheed Martin Solar and Astrophysics Laboratory, Palo Alto, CA 94304, USA and

⁴ Bay Area Environmental Research Institute, Petaluma, CA, USA

Draft version September 28, 2021

ABSTRACT

Cool and dense ejections, typically H α surges, often appear alongside EUV or X-Ray coronal jets as a result of the emergence of magnetized plasma from the solar interior. Idealized numerical experiments explain those ejections as being indirectly associated with the magnetic reconnection taking place between the emerging and preexisting systems. However, those experiments miss basic elements that can importantly affect the surge phenomenon. In this paper we study the cool surges using a realistic treatment of the radiation transfer and material plasma properties. To that end, the Bifrost code is used, which has advanced modules for the equation of state of the plasma, photospheric and chromospheric radiation transfer, heat conduction and optically thin radiative cooling. We carry out a 2.5D experiment of the emergence of magnetized plasma through (meso)granular convection cells and the low atmosphere to the corona. Through detailed Lagrange tracing, we study the formation and evolution of the cool ejection and, in particular, the role of the entropy sources: this allows us to discern families of evolutionary patterns for the plasma elements. In the launch phase many elements suffer accelerations well in excess of gravity; when nearing the apex of their individual trajectories, instead, the plasma elements follow quasi-parabolic trajectories with acceleration close to g_{\odot} . We show how the formation of the cool ejection is mediated by a wedge-like structure composed of two shocks, one of which leads to the detachment of the surge from the original emerged plasma dome.

Subject headings: magnetohydrodynamics (MHD) – methods: numerical – Sun: atmosphere – Sun: chromosphere – Sun: corona – Sun: flares

1. INTRODUCTION

Cool, chromospheric-temperature ejections are key dynamical elements of the solar atmosphere. Surges, in particular, usually appear in connection with magnetic flux emergence episodes, in which they are often associated with hot, high-speed EUV or X-ray jets. Even though observationally known for several decades now, understanding of the surges has progressed slowly and there are still many unsolved questions. First detections of chromospheric surges date back to the 1940s, when they were described as H α absorption markings related with bright eruptions (flares) corresponding to outward velocities followed by inward motion (Newton 1942; Ellison 1942). Further observational properties were obtained in the 1970s and 1980s (Kirshner & Noyes 1971, Roy 1973, Cao et al. 1980, Schmieder et al. 1984, among others): the surges were seen as blue and red shifted absorptions in H α that have a length of, typically, 10 – 50 Mm, and line-of-sight velocities of a few to several tens of km s⁻¹, reaching, in extreme cases, 100 – 200 Mm and 200 km s⁻¹ respectively. The surges were also observed in Ca II (Rust 1976); a close relationship between H α surges and EUV ejections was found as well (Schmahl 1981). Later, different observations focused on the role of the magnetic field, suggesting that the H α surges could be an indirect result of flux emergence processes and the interaction (possibly reconnection) of the upcoming magnetized plasma with the ambient coronal field (Kurokawa & Kawai 1993, Schmieder et al. 1995,

Canfield et al. 1996, Chae et al. 1999). Those suggestions were based mainly on the detection of the cool ejections next to emerging bipolar regions and quasi-simultaneously with hot coronal plasma jets (observed in the EUV or in X-rays). The high resolution observations of the past decade (e.g., Yoshimura et al. 2003; Jibben & Canfield 2004; Brooks et al. 2007; Jiang et al. 2007; Uddin et al. 2012; Vargas Domínguez et al. 2014) have provided further evidence for the frequent relation between magnetic flux emergence, chromospheric ejections and hot jets. Other chromospheric-temperature ejections such as macrospicules show some analogies with the surges: they are multithermal structures observed mainly in He II 304 Å and H α , with a cool core surrounded by a thin sheath of $1 - 2 \times 10^5$ K (e.g., Bohlin et al. 1975; Habbal & Gonzalez 1991; Pike & Harrison 1997; Madjarska et al. 2006; Bennett & Erdélyi 2015).

Concerning the theoretical effort, the seminal paper by Heyvaerts et al. (1977) (see also Forbes & Priest 1984) discussed how the emergence of magnetized plasma from the solar interior could lead to a conflict of magnetic orientation with the preexisting coronal field and hence to reconnection and the ejection of hot plasma. Using this flux emergence paradigm, Shibata et al. (1992) and Yokoyama & Shibata (1995, 1996) then showed, through a 2.5D numerical model with initial uniform coronal field, that cool plasma could be ejected next to a hot jet as a consequence of the emergence of magnetic flux from the interior: the authors tentatively identified those cool ejections with H α surges and described them as resulting from *the sling-shot effect due to reconnection, which pro-*

duces a whip-like motion (Yokoyama & Shibata 1996). Their cool surge had density around 10^{-11} g cm $^{-3}$, speeds in the range $\approx 50 - 90$ km s $^{-1}$, and maximum vertical size of several Mm. Nonetheless, due to the computational limitations of the time, the corona used in the experiment had unrealistic values of density and temperature. Using the same sort of setup but with more realistic coronal parameters, Nishizuka et al. (2008), through morphological image comparisons, suggested that the cool ejections associated with flux emergence could be the cause for jet-like features seen in Ca II H+K observations. The more recent flux-emergence experiment of Jiang et al. (2012) had a canopy-type configuration of the ambient coronal magnetic field, and also led to the ejection of cool and hot plasma. A study in three dimensions of the cool ejection following magnetic flux emergence has been published only recently (Moreno-Insertis & Galsgaard 2013). This experiment yielded a cool (from 10^4 K to a few times 10^5 K) and dense (between 10^{-12} and 10^{-13} g cm $^{-3}$) wall-like plasma domain surrounding the emerged flux region. Through Lagrange tracing, the authors explained the formation of the wall through plasma which was being transferred from the emerged region attached to field lines that change connectivity in the main reconnection site. The cool ejecta had speeds of typically less than 50 km s $^{-1}$ and were not collimated.

All those theoretical models, whether 2D or 3D, have been helpful in providing basic indications for the mechanisms that may lead to the simultaneous ejection of cold and hot plasma; nevertheless, they lack essential physical processes relevant in the photosphere, chromosphere and corona, and can therefore only be taken as first steps when trying to understand the physics of the surges. The aim of the current paper is to provide a new perspective of the cool ejections introducing some of those physical processes, like thermal conduction, photospheric and chromospheric radiative transfer, optically thin radiative cooling and a realistic equation of state (EOS). To that end we use as computational tool the Bifrost code (Gudiksen et al. 2011). For a first approach, in this paper we are using a 2.5D setup. The initial phase of the flux emergence process takes place through solar-like granular convection, which influences the sizes of the resulting structures in the low atmosphere. We can study the subsequent phenomena of reconnection and plasma ejection in the atmosphere with high temporal cadence and spatial resolution, focusing on the formation, maximum development and decay phases of the surge. The study includes detailed Lagrange tracing of the mass elements in the surge, which allows us to analyze in detail their origin and thermal evolution, the role of the various entropy sources and the acceleration mechanisms. We show that the cool and dense ejection is a complex and fascinating phenomenon in which the entropy sources play an important role.

The layout of the present paper is as follows. Section 2 describes the physical and numerical model. In Section 3 we show the initial phases of the experiment prior to the initiation of the cool ejection. Sections 4 and 5 analyze the surge in detail through its various phases (ejection, detachment and decay), focusing on the heating sources, kinematics and dynamics of the plasma elements. Finally, Section 6 contains the discussion and the summary.

2. THE PHYSICAL AND NUMERICAL MODEL

2.1. *The numerical code*

The experiment we present in this paper has been run using the radiation-magnetohydrodynamics (RMHD) Bifrost code (Gudiksen et al. 2011). This code includes thermal conduction along the magnetic field lines and radiation transfer adequate to the photosphere, chromosphere and corona; it takes into account entropy sources such as Spitzer thermal conductivity, optically thin cooling, and radiative losses by neutral hydrogen, singly-ionized calcium and magnesium, among others; details are provided in the papers by Skartlien (2000), Hayek et al. (2010), Gudiksen et al. (2011), Leenaarts et al. (2011), and Carlsson & Leenaarts (2012). The code also has an equation of state (EOS) that includes the ionization/recombination of the relevant atomic species. On the other hand, because of the validity range of the radiation tables in the code, there is an ad-hoc heating term that forces the plasma to stay above $T = 1660$ K (a discussion in detail concerning this term can be found in the paper by Leenaarts et al. 2011). The advantages of the Bifrost code probably make the simulation in this paper the most realistic one to date for the formation and dynamics of surges (but see the discussion concerning various limitations of the present model in Section 6.3).

The description of the model underlying our experiment, is divided into two parts: (1) the background stratification, numerical grid and boundary conditions and (2) the twisted magnetic tube.

2.2. *Background stratification, numerical grid and boundary conditions*

Concerning the background stratification, we started from a preexisting statistically stationary magnetoconvection configuration that includes in a self-consistent manner the uppermost layers of the solar interior, the photosphere, the chromosphere, the transition region, and the corona. The convection patterns range between granular and mesogranular. The corona has a temperature of about 1 MK and a quasi-uniform vertical magnetic field of 10 G in order to mimic a coronal hole medium. The initial magnetic field is contained in the $x-z$ plane, with z being the vertical coordinate. The left panel in Figure 1 shows the horizontal averages for our initial condition for density ρ , gas pressure P_g and temperature T , all of them normalized to their photospheric values at $z = 0$ Mm, namely, $\rho_{ph} = 3.09 \times 10^{-7}$ g cm $^{-3}$, $P_{gph} = 1.11 \times 10^5$ erg cm $^{-3}$ and $T_{ph} = 5.62 \times 10^3$ K. In the right panel we present a 2D temperature map where a number of magnetic field lines have been superimposed in black. In the image, the granulation pattern is distinguishable through the vertical field concentrations in the convective downflows and through the horizontal field lines in the center of the granules in the photosphere.

The physical domain is $0.0 \text{ Mm} \leq x \leq 16.0 \text{ Mm}$ and $-2.6 \text{ Mm} \leq z \leq 14.4 \text{ Mm}$, with $z = 0$ Mm corresponding to the solar surface, or more precisely, to the horizontal level where $\langle \tau_{500} \rangle = 1$. The numerical box has 512×512 points in the (x, z) directions respectively. The grid is uniform in the x -direction with $\Delta x = 31$ km, and non-uniform in the vertical direction in order to better resolve the lower photosphere. The vertical grid spacing varies between 19 km, reached in the photosphere and

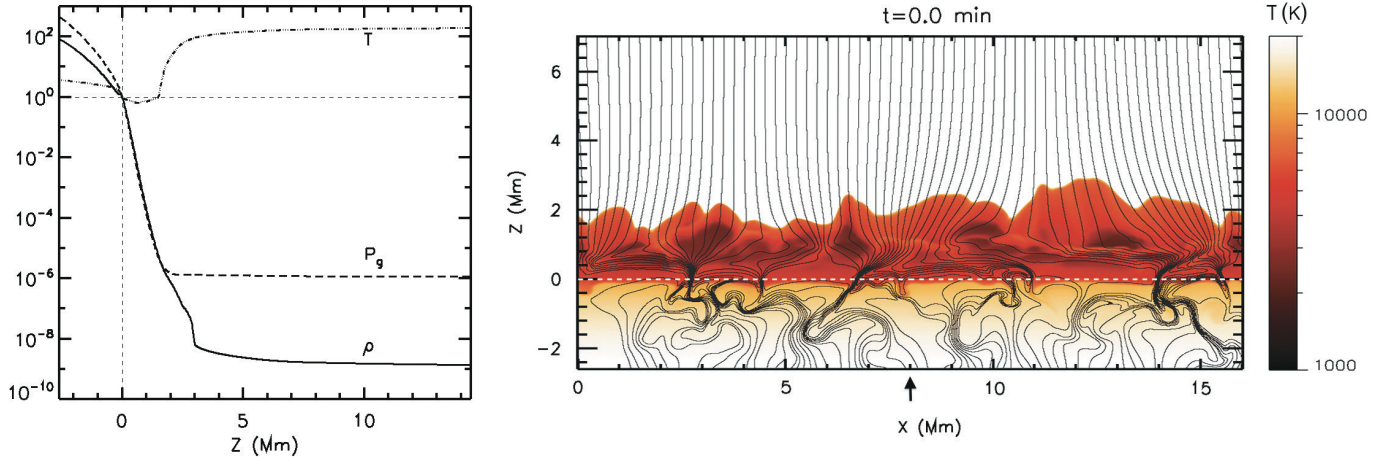


FIG. 1.— Left: Horizontal averages for density ρ , gas pressure P_g , and temperature T for the initial stratification. The values are normalized to their photospheric values at $z = 0$ Mm, namely, $\rho_{ph} = 3.09 \times 10^{-7}$ g cm $^{-3}$, $P_{gph} = 1.11 \times 10^5$ erg cm $^{-3}$, and $T_{ph} = 5617$ K. The dotted horizontal line delineates the unity and the vertical one, the solar surface. Right: Temperature map for the initial background stratification for heights between $z = -2.3$ Mm and $z = 7.0$ Mm. Magnetic field lines appear superimposed in black. The inflow region where the tube has been injected is at $x = 8$ Mm (black arrow). The solar surface is roughly at $z = 0$ Mm (dashed horizontal white line).

chromosphere, and 90 km at the top and bottom of the domain. The boundary conditions are periodic in the horizontal direction. At the top of the box characteristic boundary conditions (as described by Gudiksen et al. 2011) have been chosen that suppress incoming waves so as to eliminate any signal reflexion while the plasma can leave the domain. Additionally, the corona is expected to have temperatures of order 1 MK but the two-dimensional nature of this experiment prevents a self-consistent magnetic heating resulting from photospheric field line braiding, as in the 3D experiment of Gudiksen & Nordlund (2005). To alleviate this problem, a *hot-plate* is implemented at the top boundary, meaning a Newton cooling term that forces the temperature in the boundary cells to stay fixed at 10^6 K. For the bottom boundary the code uses a technique often implemented in magnetoconvection simulations (e.g., Stein & Nordlund 1998; Hansteen et al. 2007), namely, it keeps the bottom boundary open so that plasma can go across it, and constant entropy is set in the incoming material to keep the convection going, while the rest of the variables is extrapolated.

2.3. The twisted magnetic tube

In order to produce magnetic flux emergence, we inject a twisted magnetic tube with axis pointing in the y -direction, the ignorable coordinate in this 2.5D experiment. The injection is done through the lower boundary of the box following the method described by Martínez-Sykora et al. (2008). The longitudinal and transverse components of the magnetic field in the tube have the canonical form of a Gaussian profile with r -independent pitch (e.g. Fan 2001),

$$B_y = B_0 \exp\left(-\frac{r^2}{R_0^2}\right), \quad (1)$$

$$B_\theta = q r B_y, \quad (2)$$

TABLE 1
PARAMETERS OF THE INITIAL TWISTED MAGNETIC TUBE.

x_0 (Mm)	z_0 (Mm)	R_0 (Mm)	q (Mm $^{-1}$)	B_0 (kG)
8.0	-2.9	0.16	2.4	19

where r and θ are the radial and azimuthal coordinates relative to the tube axis, R_0 is a measure for the tube radius, q a constant twist parameter, and B_0 the magnetic field in the tube axis. To favor the emergence, we inject the tube in an inflow region, namely $x_0 = 8.0$ Mm (marked with a black arrow in the right panel of Figure 1). The rest of the parameters are selected within the ranges that lead to a coherent emergence pattern at the surface; the chosen values are presented in Table 1. The initial axial magnetic flux is $\Phi_0 = 1.5 \times 10^{19}$ Mx, which is in the range of an ephemeral active region (Zwaan 1987). This magnetic field configuration has positive helicity. The field lines have pitch $\Delta y_p = 2\pi/q = 2.6$ Mm independently of the radius. In other words, all field lines execute two turns around the axis along a distance of 5.2 Mm.

3. INITIAL PHASES

We call *initial phases* the time interval when the injected magnetic flux is rising through the convection zone and the photosphere until it reaches the low corona, or more precisely, until an emerging plasma dome is formed, as explained in Section 3.3. The initial phases share similarities with previous RMHD experiments of magnetic flux emergence (Cheung et al. 2007, Martínez-Sykora et al. 2008, Tortosa-Andreu & Moreno-Insertis 2009) and also with more idealized MHD experiments (Yokoyama & Shibata 1996, Magara 2001, Fan 2001, Archontis et al. 2004, Moreno-Insertis et al. 2008, Moreno-Insertis & Galsgaard 2013). Figure 2 illustrates the module of the magnetic field, B , at four different instants of the initial phases. In the following, we explain the different panels of the figure.

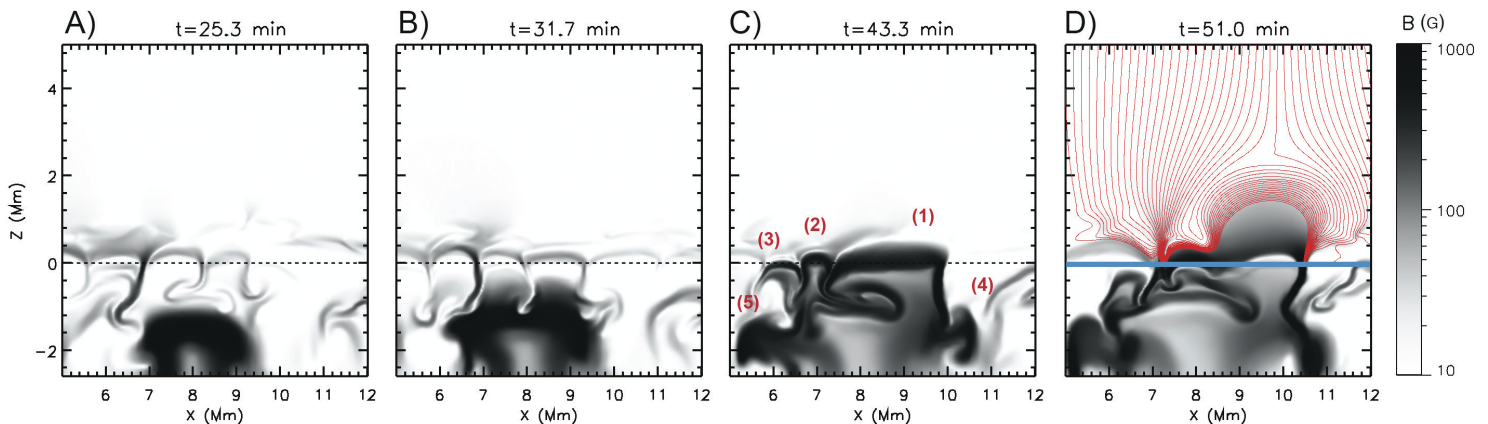


FIG. 2.— Grey-scale maps of the magnetic field strength for the initial phases of the experiment. The horizontal dashed line corresponds to the solar surface. In panel C, we have indicated with labels 1 through 5 the different fragments resulting from the initial tube. Panel D is subdivided into two parts, above and below the thick blue line: magnetic field lines are superimposed in red, but only in the upper subpanel, to avoid blurring the structures of the interior.

3.1. Emergence through the convection zone

The first stage of the rise of the magnetic tube is an expansion away from the injection point with velocities of order 1 km s^{-1} . As the tube rises through the convection zone, it starts to develop a dumbbell shape that is easily identifiable because of the high field concentration on either side of the tube axis, panel A in Figure 2. Afterwards (Panel B), the action of the convection flows on the rising tube starts to be evident. They deform and break the twisted magnetic tube into smaller fragments in the regions of strong shear, typically where the downflows hit the tube. We can identify five large fragments during the emergence process. One of the fragments of the tube, the one tagged “(1)” in panel C, reached the surface approximately 35 minutes after the initiation of the experiment. At that instant, this fragment had a horizontal size of 1.3 Mm, i.e., on the order of a granular size. Two further pieces, “(2)” and “(3)”, get to the surface at $t \sim 38$ and 43 min respectively, although they are smaller than the previous one. The fragments labeled “(4)” and “(5)” were strongly braked and pushed down by the convection downflows, and they do not reach the surface. Most of the eruptive phenomena observed in the atmosphere after the emergence are associated with the first fragment, so we focus attention onto it in the following.

3.2. Anomalous granulation and buoyancy instability

Once in the photosphere, in the transition between super- and sub-adiabatically stratified regions, the magnetized plasma starts to pile up, consequently increasing the magnetic pressure. The enhanced pressure produces a sideways growth of the fragment leading to an anomalous granule of about 2.6 Mm horizontal extent (Figure 2, panel C, $x = 7.4$ to 10 Mm), which is twice the size it had when it reached the surface. Similar anomalous granulation related with flux emergence was found in the numerical experiments by Cheung et al. (2007), Martínez-Sykora et al. (2008), and Tortosa-Andreu & Moreno-Insertis (2009), and in the observations by Orozco Suárez et al. (2008), Guglielmino et al. (2010), and Ortiz et al. (2014), among others. The later evolution of the anomalous granule occurs in the frame of the buoyancy insta-

bility (Newcomb 1961), along the general lines described by Tortosa-Andreu & Moreno-Insertis (2009) and, to some extent, also in idealized models without radiation (see Magara 2001; Archontis et al. 2004; Moreno-Insertis 2006; Murray et al. 2006). In all those cases the development of the instability allows the magnetized plasma to rise well above the photospheric heights.

3.3. The emerged magnetized dome

Following the buoyancy instability, the plasma belonging to the anomalous granule suffers a rapid expansion into the atmosphere with radial velocities of 15 km s^{-1} at heights around 1 to 2 Mm. This expansion leads to the classical dome (or mountain) formation already found in the past (see, e.g., Yokoyama & Shibata 1996, Archontis et al. 2004, Moreno-Insertis & Galsgaard 2013 and references therein). In panel D of Figure 2 we show the early stages of the emerged dome, between $z = 0$ Mm and $z = 2$ Mm approximately. In the upper subpanel (above $z = 0$, marked by a thick horizontal line in blue), magnetic field lines are shown superimposed in red: they are seen to collect into compact field line bunches at the location of photospheric downflows. One of those bunches is located at $x \approx 7.2$ Mm; the region between those lines and the left side of the dome corresponds to a current sheet that is described in Section 3.4.

As the dome expands, and as expected for expansion phenomena in the chromosphere (e.g. Hansteen et al. 2006; Martínez-Sykora et al. 2008; Tortosa-Andreu & Moreno-Insertis 2009; Leenaarts et al. 2011), the plasma temperature decreases significantly, reaching the lower limit allowed in our simulation explained in Section 2. Simultaneously, the dome interior suffers a draining process owing to the gravitational flows that take place along the loop-like magnetic field lines, as described by Moreno-Insertis & Galsgaard (2013). The combination of the expansion and the draining produces a density change from the values during the first stages of the dome evolution (10^{-11} to $10^{-12} \text{ g cm}^{-3}$) to values on the order of $10^{-14} \text{ g cm}^{-3}$ in later phases.

3.4. The current sheet: unsteady reconnection

The expansion of the dome pushes its magnetic field against the preexisting vertical coronal magnetic field. This generates an orientation conflict on the left-hand side of the dome, giving rise to a thin concentrated current sheet. In Figure 3, we illustrate the latter using as inverse characteristic length of the magnetic field variation the quantity

$$L_B^{-1} = \frac{|\nabla \times \mathbf{B}|}{|\mathbf{B}|}. \quad (3)$$

This quantity permits good visualization of any abrupt change of B . For comparison, in a pure rotational discontinuity of the field L_B^{-1} is π times the inverse width of the sheet while in a Harris sheet it goes through infinity at the center of the sheet. In the figure, the pixels where $L_B < 1000$ km are shown in color, with magnetic field lines superimposed as solid lines. There is a reconnection site located at $x \sim 6.8$ Mm and $z \sim 1.8$ Mm (black cross). Along its lifetime, the current sheet repeatedly experiences the formation of plasmoids (like the one at $z \sim 2.4$ Mm in Figure 3) through the development of the tearing-mode-instability (Furth et al. 1963). This behavior has been detected in previous flux emergence experiments, e.g., in 2D by Yokoyama & Shibata (1996), and in 3D by Archontis et al. (2006), Moreno-Insertis & Galsgaard (2013) and Archontis & Hansteen (2014). In our case, the timescale of plasmoid formation is between several tens of seconds and a few minutes. This range is compatible with the theoretical value for the growth time of the tearing mode (see Goldston & Rutherford 1995): the latter is close to the geometric mean between $\tau_a = L_B/v_a$ and $\tau_d = L_B^2/\eta$, where v_a is the Alfvén velocity and η is the diffusivity. In our current sheet, $\tau_a = 10^{-2} - 10^{-3}$ s, and $\tau_d = 10^7 - 10^8$ s, and the geometric mean of those quantities is near the measured values in the experiment.

As time goes on, the area where the orientation conflict is located grows in length because of the dome expansion. During this phase, the plasmoids are ejected as part of the reconnection process, probably through the melon seed ejection mechanism (Schlüter 1957), which can be launched when there is an imbalance in the Lorentz force holding the plasmoid on its sides along the current sheet. Some of the plasmoids also merge forming bigger ones as a result of the coalescence instability (Finn & Kaw 1977).

4. THE EJECTION OF COOL, HIGH-DENSITY PLASMA

As a result of the reconnection process taking place at the boundary between emerged dome and coronal material, a substantial amount of plasma with chromospheric temperatures and densities is ejected to coronal heights. We refer to this phenomenon as the *cool and dense ejection* or *surge* and avoid the word *jet*, since the ejecta are not collimated and do not have large speeds, as shown in this section. In Figure 4, the overall evolution of the surge from the initial stages to the decay phase is illustrated using grayscale maps for the density and with a number of temperature contours with values indicated in panel A. In panels A and B we can see an apparent peeling process that is carrying dense and cool plasma to greater heights toward the right of the dome. At the

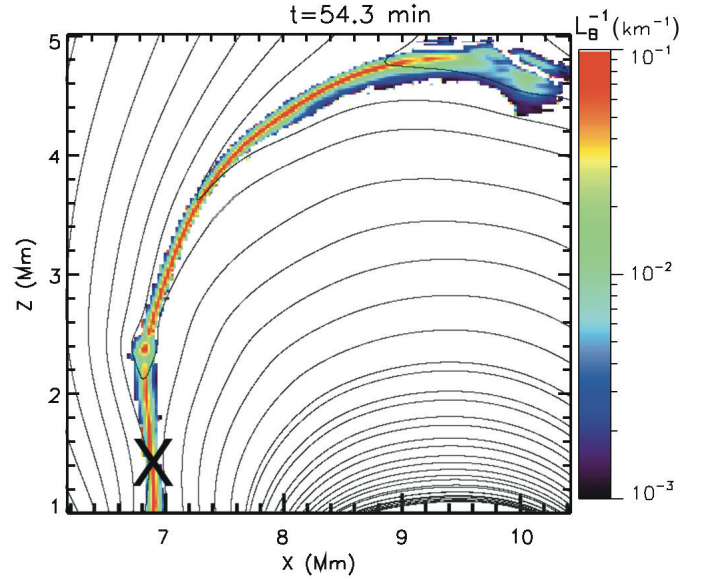


FIG. 3.— Map of the inverse characteristic length of the magnetic field L_B , see Equation (3), illustrating the thin current sheet at the boundary between emerged plasma and the corona. Only the pixels where $L_B < 1000$ km are shown in color. Magnetic field lines appear superimposed as solid lines. The black cross is the central part of the reconnection site.

same time, a hot coronal jet is forming on the left side as can be identified through the pink contours in Panel B. In panel C, the dome seems to be splitting into two parts at $x \approx 12$ Mm. In panel D, we can distinguish the cool and dense plasma ejection as the elongated structure located to the right of the emerged dome with temperatures below 3×10^4 K, i.e., chromospheric temperatures, including a colder core of lower temperatures down to 2×10^3 K. Around this instant, the ejecta reach their maximum height, $z = 13.2$ Mm, and the density range in the surge is between 10^{-14} g cm $^{-3}$ and 10^{-11} g cm $^{-3}$. The rest of the panels (E, F, G and H) show the decay phase. During the decay, the surge moves first to the left and then to the right in a swaying motion caused by the Lorentz force associated with the bending of its magnetic field lines. The cool surge remains as an easily identifiable feature until $t \approx 66$ min, so its lifetime can be estimated to be about 7–8 minutes. The accompanying Movie 1 shows the time evolution of the density and temperature of the system.

In order to analyze the fundamental aspects of the surge, we have followed more than 3×10^5 plasma elements through Lagrangian tracing. The choice of tracers was carried out at the time of maximum vertical extent of the cool ejection, $t = 61$ min, and is shown in panel I of Figure 5 with dots of different colors superimposed on the image. We set the side and top boundary of the surge to coincide with the isocontour $T = 3 \times 10^4$ K (blue curve) and use as lower limit the $z = 2$ Mm horizontal axis. The tracers are then evenly distributed in that domain with high-resolution spacing $\delta x = \delta z = 10$ km. For later reference, we have drawn the tracers in four different colors (cyan, yellow, purple and red) according to the four different populations of plasma elements that are introduced and discussed from Section 4.1 onward. The resolution is high enough for the individual tracers

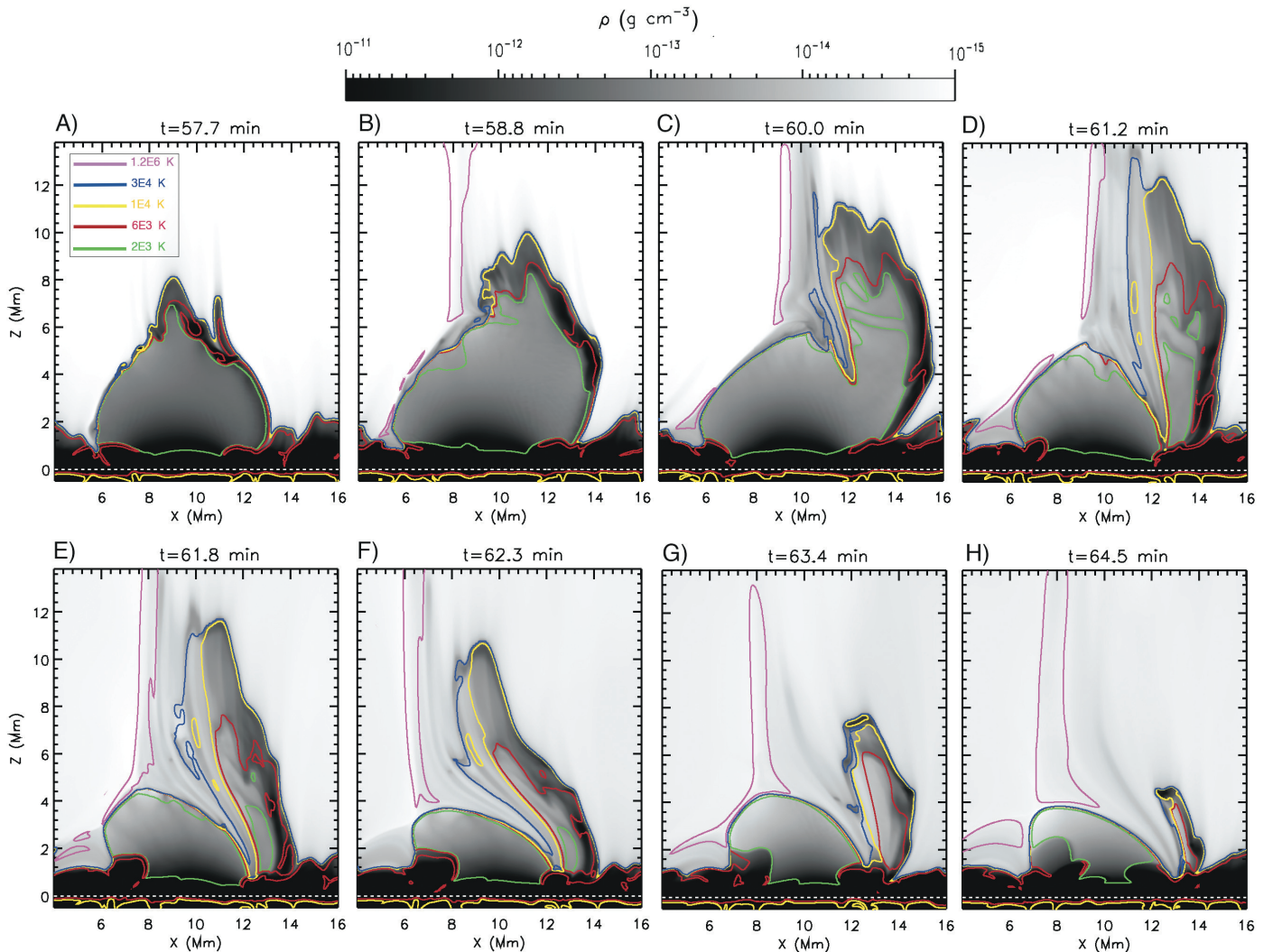


FIG. 4.— Density maps showing the formation and descending phases of the cool and dense ejection. Temperature contours have been superimposed to the maps to complete the image: the association of colors to temperatures is given in panel A. The hot coronal jet is also visible on the left-hand side of the dome delineated by the pink contours. See also the accompanying Movie 1.

to be indistinguishable in the figure: the domains look like a continuous surface. Once the distribution is established, we follow the tracers backward in time until $t = 51$ min, to study their origin, and also forward, until $t = 65$ min. The tracking has a high temporal cadence of 0.2 seconds in order to reach good accuracy even in locations with high gradients and phases of fast changes, like when going through the current sheet.

The rest of this section is divided into three blocks devoted to the heating and cooling sources of the surge (Section 4.1), the plasma acceleration (Section 4.2), and the velocities, densities and temperatures (Section 4.3).

4.1. Heating and cooling sources

Here we analyze the heat sources and sinks in the surge, since they are key for understanding its structure and evolution. From all the entropy sources included in the Bifrost code, the relevant ones for the surge are those resulting from the Spitzer thermal conductivity, the optically thin cooling, the radiative losses by neutral hydrogen, and the ohmic and viscous heating. The rest,

like those associated with the chromospheric radiative losses by singly-ionized calcium and magnesium, have much longer characteristic times and need not be discussed. The following results are focused on the rising phase of the ejecta until they reach their maximum height at around $t = 61$ min. Thereafter, the characteristic times of the heating and cooling processes become much longer than the general evolutionary timescale of the surge: the temperature changes in the decay phase are due to adiabatic compression.

The study of the thermal properties of the individual Lagrangian elements allows one to discern four different plasma populations within the ejecta of different origin and evolution that we have identified with labels “A”, “B”, “C” and “D”, and drawn in colors cyan, yellow, purple and red, respectively, in Figure 5. In Panel I we have already introduced the distribution of the Lagrangian elements when the cool ejection reaches its maximum height. Panels II.1 – II.4 show the evolution of those elements during previous stages of the surge. These panels illustrate the origin of the plasma in the surge and how

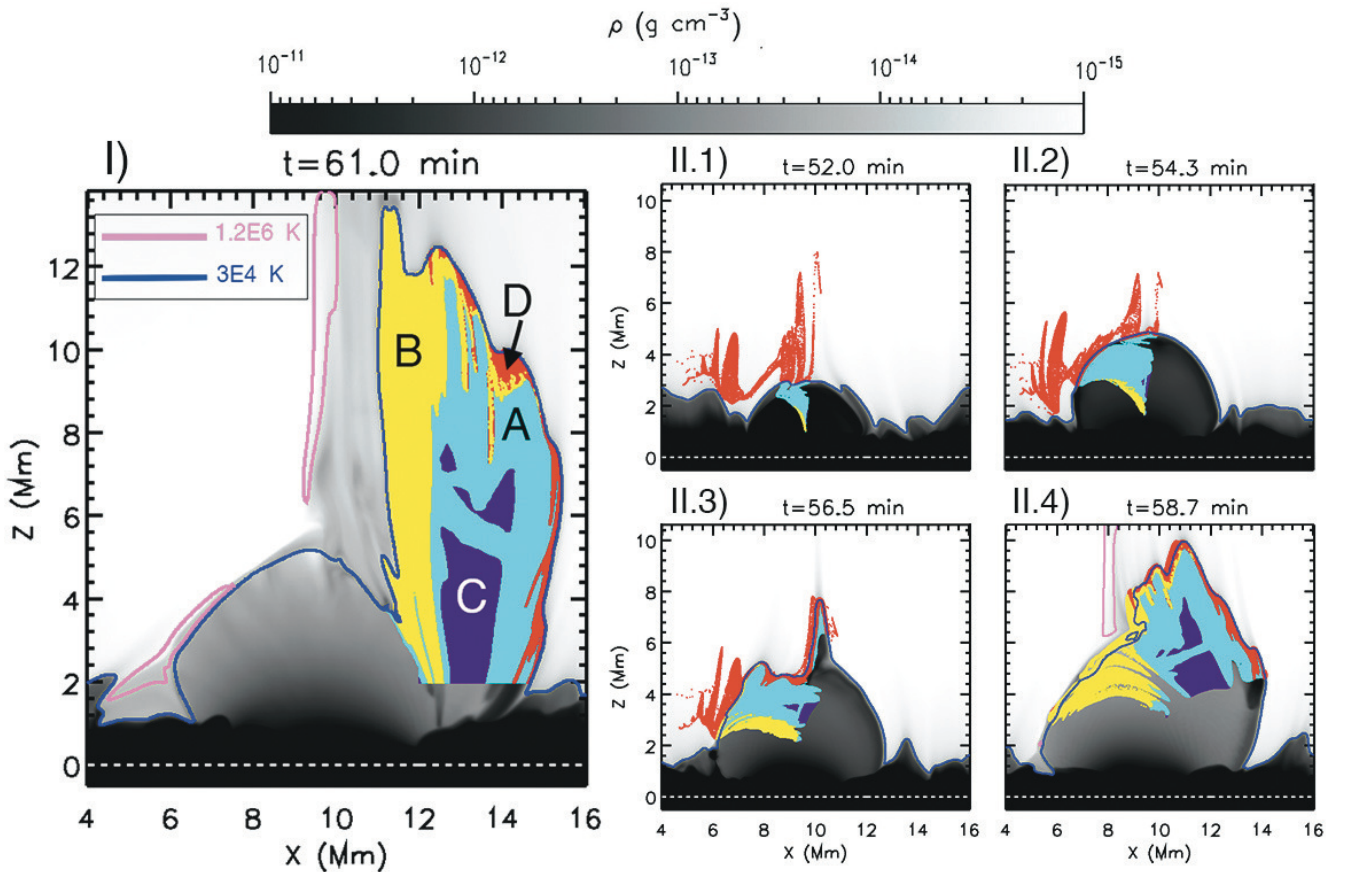


FIG. 5.— Panel I: Density map showing the basic distribution of the more than 3×10^5 Lagrangian tracers by means of colored domains (cyan, yellow, purple and red). The domains correspond to the four different populations discussed from Section 4.1 onward and are tagged with the corresponding capital letters. Panels II.1 through II.4: Evolution of the ensemble of tracers from time 52 min onward. A more continuous illustration of the time evolution is given in the accompanying Movie 2).

the different populations evolve to give rise to the distribution shown in Panel I. A more complete view of the formation of the surge is also provided via the accompanying Movie 2. The nature of the different populations is analyzed in the following.

4.1.1. Population A

Population A, plotted in cyan in Figure 5, corresponds to plasma originating in the dome (see panel II.1) and it is heated through Joule and viscous dissipation during the early stages of formation of the surge. Owing to the high density of this population, those entropy sources are not able to heat the plasma to values above 3×10^4 K. At $t = 61$ min, this population covers 44% of the cross section of the surge and its total mass per unit length in the y direction is 10^{-3} g Mm $^{-1}$. The top-left panel in Figure 6 shows with a black solid line the time evolution of the temperature of a representative plasma element of this population. The element jumps from dome temperatures, close to 2×10^3 K, to values around the temperature of the hydrogen ionization/recombination, namely 6×10^3 K. In the same panel (red curve), the values of L_B^{-1} at the positions reached by that plasma element indicate that it passes near the current sheet, but not quite through it: the typical values of L_B in the current sheet are less than 100 km (see Figure 3).

4.1.2. Population B

The second group of Lagrange tracers is what we call Population B, drawn in yellow in Figure 5. Its defining feature is that the plasma elements in it, in spite of originating in the dome, reach temperatures between 10^5 and 10^6 K during the launch phase, and then cool down to temperatures below 3×10^4 K. This family leaves the dome later than the elements of population A, as shown in the panels II.1 – II.4 of Figure 5; it ends up covering 34% of the surge’s cross section at $t = 61$ min, but it has comparatively low densities, so its integrated mass at that time is 4.7×10^{-5} g Mm $^{-1}$ only. There are two main reasons for the sudden increase in temperature of the elements of this population, namely:

1. Unlike for Population A, some of its plasma elements pass through the current sheet, and are strongly heated there (see the yellow tracers above the blue temperature contour, 3×10^4 K, in panels II.3 and II.4). The top-right panel in Figure 6 depicts an example of this behavior for a representative member of this population. The characteristic length L_B reaches a small value, around 25 km, after which it decreases, indicating that the plasma element is then leaving the current sheet. When in the current sheet, the Joule dissipation and, to a lesser extent, the viscous dissipation become highly efficient, with short characteristic timescales from

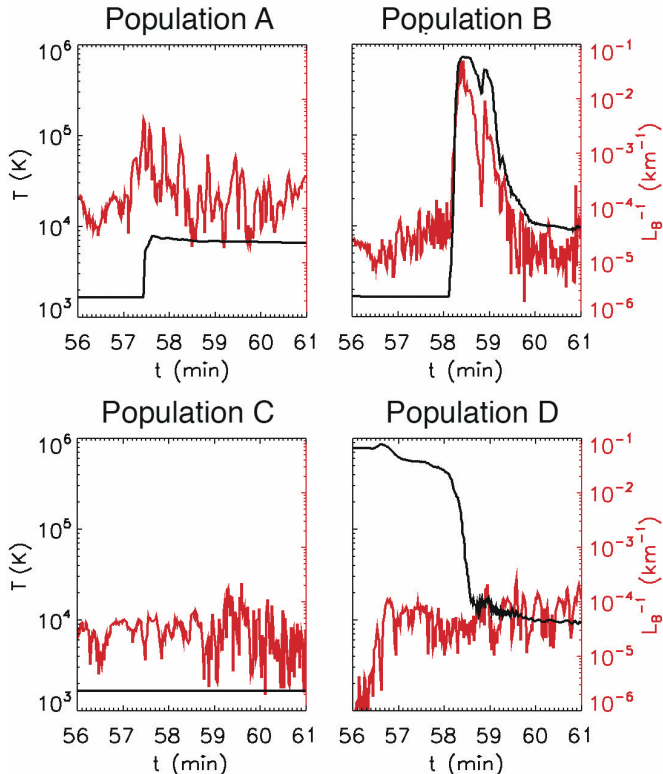


FIG. 6.— Set of panels showing the time evolution for four different plasma elements followed by Lagrangian tracing. The chosen elements are representative of the four different populations we found concerning the thermal properties. In the panels, the temperature T is plotted in black while L_B^{-1} in red. This last quantity allows to identify the proximity of the element to the current sheet.

several seconds to a few tens of seconds, as shown in the left panel of Figure 7.

2. Some plasma elements of this Population, those close to the blue contour on the left side of the surge in panel I of Figure 5, are affected by their passage through a strong shock. This shock is a central feature of the dynamics of the surge and is described separately (Section 5).

Additionally to the foregoing, the heating processes are particularly effective at increasing the temperature of the particles of this population given their comparatively low initial density: their late ejection from the emerged dome implies that the density of the latter has already been substantially reduced through the gravitational draining explained in Section 3.3. The late ejection furthermore explains their appearance on the left hand side of the surge and with comparatively low density (see the left side of the surge in panel D of Figure 4 in comparison with its right side).

The short duration of the high temperature spurt of these mass elements is explained by the activation, when the temperature is nearing 10^6 K, of thermal conduction and optically thin radiative losses as effective entropy sinks. The associated characteristic times (τ_{Spitz} , τ_{thin} , respectively) for the plasma element studied above can be seen (Figure 7, right panel) to reach low values of several seconds (τ_{Spitz}) or of a few tens of seconds (τ_{thin}). When

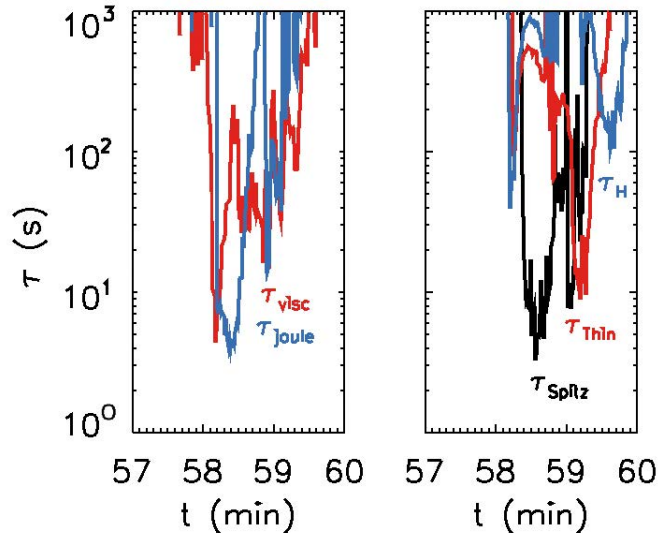


FIG. 7.— Characteristic times of the entropy sources and sinks for the representative plasma element of Population B used in Figure 6. Left panel: Joule (τ_{Joule}) and viscous (τ_{visc}) heating sources. Right panel: Thermal conduction (τ_{Spitz}), optically thin radiative losses (τ_{thin}), and radiative losses by neutral hydrogen (τ_H).

T decreases to values around 10^4 K, the radiative losses by neutral hydrogen can also be important (see the curve labeled τ_H). It is through these cooling processes that the elements of this population eventually adopt the cool temperatures of the surge.

4.1.3. Population C

Population C, plotted in purple in Figure 5, is a fraction of the surge coming from the dome that maintains its initial temperature in the time range shown. At $t = 61$ min, this population covers 15% of the cross section of the surge and has a small mass content, 2.8×10^{-5} g Mm $^{-1}$. The Lagrangian tracing shows that the plasma elements were dragged passively from the dome, following the motion of the magnetic field lines explained in Section 4.2.1. Along this process, they are never heated by Joule or viscous dissipation. The local values of T and L_B^{-1} for a representative plasma element of this population are given in Figure 6, bottom-left panel. In fact, those plasma elements expand along their motion, which explains why this population is barely visible in panels II.1 and II.2 of Figure 5 in comparison with panels II.3 and II.4). The density of the elements decreases by approximately one order of magnitude, but their temperature is kept constant through the ad-hoc heating term mentioned in Sections 2 and 6.3.

4.1.4. Population D

A small fraction of the Lagrange elements in the surge, plotted in red in Figure 5, have tracks that start in coronal heights at $t < 57$ min (panels II.1 – II.3). The ensemble of such elements is called Population D in the following. They cover 7% of the cross section of the surge at $t = 61$ min (panel I). The temperature and L_B^{-1} evolution for a representative plasma element of this population is shown in the bottom-right panel of

Figure 6. The tracks start at heights well above the reconnection site, with standard coronal temperature and density. When approaching the current sheet, though, these elements go through regions of large density gradients. The diffusion term included in the mass conservation equation becomes important, with characteristic timescale less than one minute, i.e., similar to the evolutionary time of the particles. The evolution that takes place then is effectively equivalent to a process of mixing across the density gradient with plasma elements coming from the dome, after which their behavior is equivalent to that of population A. This kind of effective mixing is peculiar of population D: the density diffusion term is small for the elements of the other populations. A proper study of the evolution of this population must therefore await a numerical experiment with much higher spatial resolution and correspondingly small numerical diffusion (see also the discussion in Section 6.3).

4.2. The acceleration of the surge

We turn now to the dynamics of the surge and study the acceleration of the plasma elements first during the launch phase (Section 4.2.1) and then when they are near the apex of their trajectory (Section 4.2.2).

4.2.1. Acceleration during the launching phase

The initial acceleration of the mass elements of the surge takes place when they are not far from the thin current sheet that covers the top-left region of the dome (Section 3.4). In this region, the Lorentz force may reach values well above gravity because of the high curvature of the magnetic field lines after reconnection. The gas pressure gradient may also reach large values because of the low values of the magnetic field at the center of the current sheet. For an estimate, call a_L and a_p the acceleration associated with those forces, use L_B as given in Equation (3) and define L_P as the corresponding length scale of variation of the gas pressure. One obtains:

$$\left| \frac{a_L}{g_\odot} \right| = \frac{v_a^2}{2L_B g_\odot} \approx 18 \frac{(v_a)_{100}^2}{(L_B)_{\text{Mm}}}, \quad (4)$$

$$\left| \frac{a_p}{g_\odot} \right| = \frac{c_s^2}{\gamma L_P g_\odot} \approx 22 \frac{(c_s)_{100}^2}{(L_P)_{\text{Mm}}}, \quad (5)$$

where the subindices “100” and “Mm” indicate velocities measured in units of 100 km s^{-1} and lengths measured in Mm, respectively, and v_a , c_s , g_\odot and γ have their customary meaning (Alfvén and sound speed, solar gravity, and ratio of specific heats, respectively). In the reconnection region, the characteristic lengths are substantially smaller than 1 Mm and either the Alfvén velocity or the sound speed (or both) are of order 100 km s^{-1} . Equations (4) and (5) tell us, therefore, that a_L and a_p can easily exceed g_\odot ; in fact, in some extreme cases they reach values of a few times $100 g_\odot$ for a short period of time.

Figure 8 shows the vertical acceleration components a_{L_z} (red) and a_{p_z} (blue) for the representative Lagrangian elements used in Figure 6. We note the following behavior:

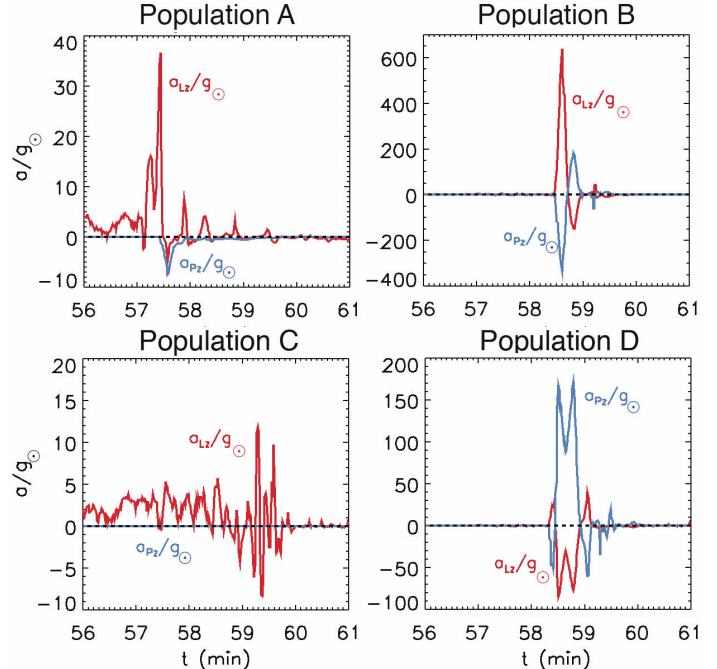


FIG. 8.— The vertical acceleration components a_{L_z} and a_{p_z} in units of g_\odot , in red and blue respectively, of the same representative plasma elements used in Figure 6. The panels illustrate the high acceleration of the plasma during the launch of the cool ejection.

- In Section 4.1.1 we saw how the elements of population A pass near, even though not quite through, the current sheet. In the top-left panel of Figure 6 we see how, in that phase, they are ejected by the Lorentz force with accelerations of tens of g_\odot . We also note the close relationship between the dynamic and thermodynamical changes (compare this panel with the corresponding one in Figure 6).
- In the case shown in the top-right panel (population B), the element is ejected upward in a short time interval around $t = 58.5 \text{ min}$. The acceleration values are extreme in this case, reaching $a_{L_z}/g_\odot = 6.4 \times 10^2$ and $a_{p_z}/g_\odot = -3.5 \times 10^2$ and last for about 10 s. Those values result from the fact that the element is going through the current sheet at that point and the characteristic lengths are correspondingly small, $L_B = 40 \text{ km}$ and $L_P = 50 \text{ km}$ (compare these lengths with those shown in Figure 3).
- The elements in Population C, like the one shown in the left-bottom panel, are the furthest away from the current sheet and their characteristic lengths are the largest ones. As a consequence, the acceleration values are lower than for other populations but are, anyway, typically a few to several times g_\odot . The plasma in this population is dragged by the magnetic field following the highly dynamical motion initiated in the current sheet and the gas pressure does not play any important role.
- The right-bottom panel shows an element from Population D. The large pressure gradients in the boundary between the corona and the current sheet

TABLE 2
STATISTICAL MOMENTS OF THE THREE DISTRIBUTIONS OF
FIGURE 9.

Curve	$t - t_{apex}$ (min)	Mean $/g_{\odot}$	$\sigma_{st dev}/g_{\odot}$	Mode $/g_{\odot}$
Black	[-1,1]	-0.99	6.3	-1.1
Red	[-2,2]	-0.48	6.6	-1.1
Blue	[-3,3]	0.18	11.	-1.0

lead to a small characteristic length $L_P = 100$ km and to the predominance of a_{p_z} compared to a_{L_z} . The extreme values of the acceleration in this case are around $a_{L_z}/g_{\odot} = -0.8 \times 10^2$ and $a_{p_z}/g_{\odot} = 1.6 \times 10^2$, and last for about 20 sec.

In the foregoing we have proved that the Lorentz force and gas pressure gradients in the region at and near the current sheet can easily cause substantial accelerations of tens to hundreds of g_{\odot} . This may seem quite large, but it is naturally associated with the fact that the plasma elements must jump by, in some cases, 6 Mm in height (from the top of the dome to the top of the resulting surge, check Figure 4) in a matter of, say, one minute. As an elementary calculation shows, sustained accelerations of several times g_{\odot} (or impulsive accelerations of from tens to hundreds of times g_{\odot}) ought to be expected.

4.2.2. Acceleration near the apex of the trajectories

We examine now the acceleration of the plasma elements during the central period of development of the surge, namely when the Lagrange elements are close to the apex of their trajectories. To do this, we call t_{apex} the time when each individual element reaches its maximum height and use $t - t_{apex}$ as time variable. Figure 9 contains three histograms for the vertical accelerations of the plasma elements for $|t - t_{apex}| = 1$ min (black curve), 2 min (red curve), and 3 min (blue curve). Additionally, we have carried out a statistical study using the sample of the vertical accelerations of all elements during the indicated time intervals with a cadence of 0.2 s. The basic moments of the statistical distribution and their mode are given in Table 2. The three distributions are highly peaked (positive kurtosis) and their most frequent value (the mode) is very near $-g_{\odot}$ in all cases. The mean of the most representative histogram (black curve) also coincides with $-g_{\odot}$. Yet, the distributions are not narrow, with standard deviations ranging from $6g_{\odot}$ to $11g_{\odot}$. Also: as wider time ranges around t_{apex} are chosen (red and blue curves), upward accelerations linked to the launch phase are more frequently represented and the mean of the distributions then shifts toward positive values.

4.3. Further properties: velocity, temperature and density

We describe now some further properties of the ejecta: velocities, temperatures and densities. Figure 10 contains double PDF plots for the vertical velocity u_z (upper row), and the density ρ (lower row) versus the temperature, T , of the Lagrangian elements. The panels illustrate representative phases of the surge: the launch phase (A panels); and the instant where the surge reaches its maximum vertical extent (B panels).

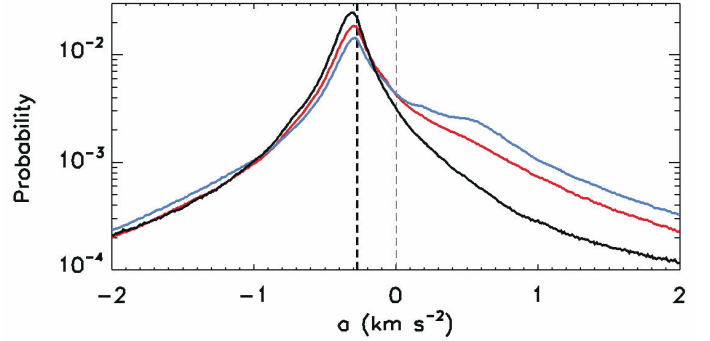


FIG. 9.— Histograms of the vertical accelerations for a time interval around the apex of the trajectories $|t - t_{apex}| = 1$ min (black curve), 2 min (red curve), and 3 min (blue curve). The vertical lines mark $-g_{\odot}$ (thick) and the zero acceleration value (thin). The statistical properties of these distributions are collected in Table 2.

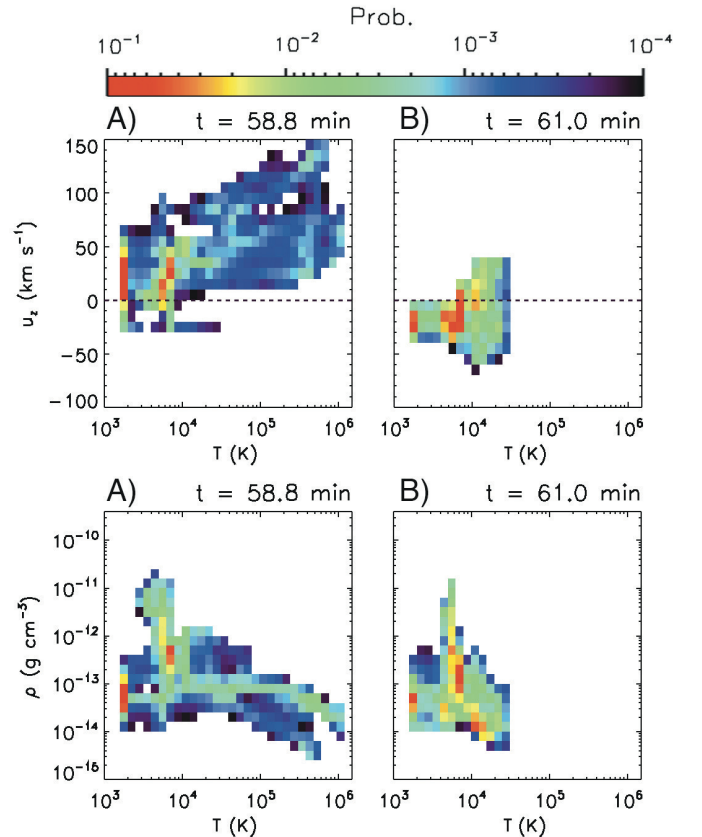


FIG. 10.— Double PDF plots for the temperature T and either the vertical velocity u_z (upper panels), or the density ρ (lower panels) of the Lagrangian elements.

- In the A panels we see that the majority of the plasma elements have cold temperatures (close to 2×10^3 K), densities around 10^{-13} g cm $^{-3}$, and velocities of a few tens of km s $^{-1}$: these are elements located in the dome at that time. Further, there is a group of elements clustered at a temperature of 6 to 7 thousand K, possibly near the phase of hydrogen ionization/recombination, with small, positive velocities also of tens of km s $^{-1}$. This group contains a mixture of elements

that have reached that temperature either through heating of cold plasma (Population A) or cooling of hot plasma (Populations B and D) through the action of the different entropy sources. Additionally, in the density panel there are two extended tails of elements toward higher temperatures and velocities. Those elements correspond to, on the one hand, hot, low density Population-D plasma originating in the corona, and, on the other hand, denser plasma from Population B undergoing its heating-cooling phase. As we saw in Section 4.2.1, the elements of Populations B and D suffer the largest accelerations and, as a consequence, the range of velocities is between 20-150 km s⁻¹.

- The B panels in the figure are representative of the phase of maximum vertical development of the ejection. We see that basically the whole ensemble is already falling, albeit with small velocities ($|u_z| < 30$ km s⁻¹). Concerning the temperatures, there is an important concentration of particles at the temperatures of hydrogen ionization/recombination (around 6×10^3 K), ionization/recombination of He I/He II (around $T \sim 10^4$ K, label “4”) and, to a lesser extent, of He II/He III (around $T \sim 2 \times 10^4$ K, label “5”) – see also the discussion about this issue in Section 6.3. The density range for this phase of the cool surge is between 10^{-14} and 10^{-11} g cm⁻³. In the later phases of the surge, the velocities continue in the range of a few to tens of km s⁻¹.

The resulting global picture of the surge during its main development phase corresponds to plasma with velocities of tens of km s⁻¹. The temperatures tend to be $0.6 - 1 \times 10^4$ K (but with a small population which have retained their original cold temperature of a few thousand K) and the densities are in a large range between 10^{-14} and 10^{-11} g cm⁻³.

5. THE DETACHMENT OF THE COOL EJECTION FROM THE DOME

Looking back at Figure 4, we realize that from panel D onward the ejecta adopt the shape of a detached *wall*, a cool and dense wall. Going a little earlier in time (panel C), we locate the origin of the detachment in the fact that the dome is being split in two at $x \approx 11$ Mm, the process taking place mainly between $z \approx 4$ and $z \approx 6$ Mm. The appearance of this *cleft* is especially noticeable following the blue temperature contour ($T = 3 \times 10^4$ K). In panels D and E, the detachment is seen to be complete and the ejecta are from then on a separate wall-like structure.

The explanation of this phenomenon lies in the formation of a series of shocks above the dome starting at $t \approx 59$ min (check also the density and temperature evolution shown in the accompanying Movie 1). Successive blobs of plasma coming up from the reconnection site along the top of the dome impinge on the surge. Strong shocks are created that deform and redirect plasma in the blob, last for a brief period of time and then weaken. A new blob arrives and creates again a shock system of the same kind. To illustrate the shock region in one of these collision events, Figure 11 (left panel: general view; right-panel: blow-up of the shock region) shows a map of

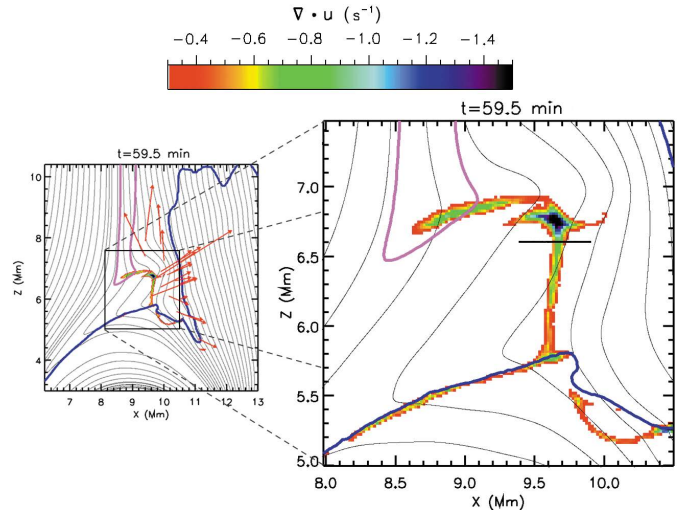


FIG. 11.— Left: Map of the velocity field divergence, $\nabla \cdot \mathbf{u}$. Only the pixels where $\nabla \cdot \mathbf{u} < -0.5$ s⁻¹ are shown in color. Pink and blue contours are the same that in Figure 4. The magnetic field is superimposed as black lines while the velocity field in the detachment region is shown with red arrows. Right: Zoom out for the previous panel to highlight the shock region. The horizontal black line is the cut used in Figure 12 to study the fast shock.

the divergence of the velocity field, $\nabla \cdot \mathbf{u}$, thus signposting the locations where a large compression is taking place. Further, the figure contains the blue (3×10^4 K) and pink (1.2×10^6 K) isotemperature contours of Figure 4, and a collection of field lines drawn as black curves. Also, the arrows show the velocity field in the detachment region, between the hot jet and the cool ejecta.

From the color map we see that the shock front has a wedge-like or arrowhead shape, which is a common feature of the successive shocks seen during the detachment phenomenon. The shocks cause high levels of compression and heating of the plasma going through it. The two sections of the arrowhead show distinctive features: the upper part, which is roughly horizontal and nearly perpendicular to the field lines in the postshock region, resembles a slow-mode shock almost of the switch-off kind. This could be related with the slow-mode shocks generated when plasmoids collide with the ambient magnetic field after being ejected, as illustrated by Yang et al. (2013). This shock is directly related with the hot jet: it is located at the base of the latter (see the pink contours) and the plasma goes through it before flowing along the horn-like jet field lines. We leave its study for a follow-up paper dealing with the properties of the hot jet.

The lower, almost vertical branch of the wedge, in turn, is a shock directly associated with the detachment process studied in this section. The field lines cross it but subtending only a small angle to the tangent direction to the shock front. $\nabla \cdot \mathbf{u}$ has high compression values of about -0.8 s⁻¹, sometimes reaching even -3.0 s⁻¹. Plasma traverses the structure from the left. Figure 12 shows the profiles across the shock for a number of relevant variables. To that end, we plot those variables along the horizontal black line plotted in the right panel of Figure 11. The B_z component (panel A) is not far from the perpendicular component of the field to the front normal. This component increases by a factor of 2 in absolute value across the shock, which suggests that the shock is a

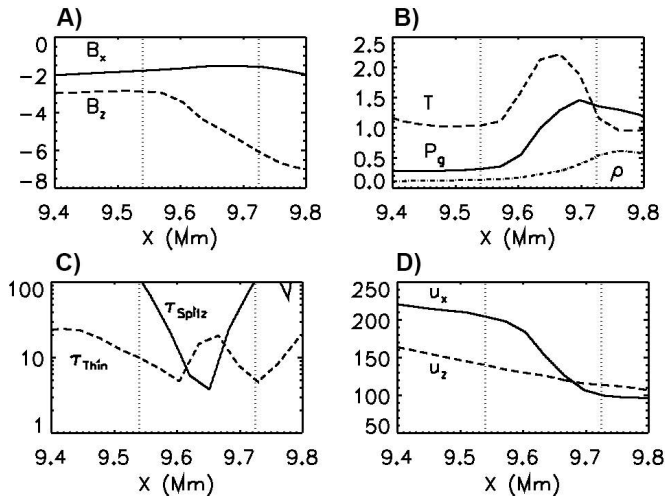


FIG. 12.— Jump relations along the horizontal black line in the right panel of Figure 11. The auxiliary vertical lines enclose the compression region where $\nabla \cdot \mathbf{u} \leq -0.2 \text{ s}^{-1}$. Panel A: Magnetic field B_x and B_z in G. Panel B: Temperature T normalized to 4×10^5 K, gas pressure P_g in erg cm^{-3} , and density ρ normalized to $10^{-13} \text{ g cm}^{-3}$. Panel C: characteristic times for the Spitzer conductivity, τ_{Spitz} , and the optically thin losses, τ_{Thin} , in seconds. Panel D: velocities u_x and u_z in km s^{-1} .

moderately strong, fast shock. This is also supported by the fact that the quasi-parallel component of the velocity (u_z , panel D) does not change substantially across the shock, whereas the normal velocity changes by a factor 2, approximately. The temperature has a suggestive profile (panel B), that we can understand with the help of the entropy sources (panel C). In the first half of the shock the temperature increases, mostly because of the compression work experienced by the plasma element when entering the shock. In the center and final half of the shock, however, T reaches a plateau and decreases: this is probably due to the action of the heat conduction (to a limited extent also of the optically thin radiation cooling): the characteristic cooling time scales are low (4 s for the former, see panel C), and fit with the duration of the transit of the plasma across the shock if one takes into account the motion of the front as a whole. Finally, the density increases by a factor 5 (panel B), which is larger than the maximum allowed for adiabatic shocks: the large compression ratio is reached thanks to the entropy decrease due to the non-adiabatic effects. As a further consequence of the heat conduction, the thermal energy is distributed efficiently along the individual field lines well beyond the shock itself, giving rise to the structure along the cleft that marks the boundaries of the cool ejection and lets it appear as a separate domain. The velocities involved in the shock, panel D, are on the order of a hundred km s^{-1} .

The plasma diverted downward after crossing the vertical section of the shock penetrates deeper into the underlying dome as successive shock systems are formed. When the last one in the series ends ($t \approx 61$ min, Panel F of Figure 4), the surge is completely detached from the remnants of the dome on the left. The hot plasma domains at that time have the classical inverted-Y or Eiffel-tower shape commonly seen in observations, with one of the legs of the tower coinciding with the *cleft*. Meanwhile, the cool surge enters the decay phase following

the swaying motion explained at the beginning of Section 4. Both the hot and cool ejections finally disappear almost simultaneously at around $t = 66$ min.

6. DISCUSSION

We have performed a 2.5D radiative-MHD numerical experiment of emergence of magnetized plasma through granular convection and into the atmosphere. The time evolution of the system leads to the ejection of part of the emerged material as a cool and dense surge. The experiment was done with the Bifrost code, which includes a realistic multi-component equation of state as well as modules for photospheric and chromospheric radiation transfer, heat conduction and optically-thin radiative cooling in the corona. In the following we first provide a comparison with observational data (Section 6.1) and then discuss the relevance of some of the entropy sources not included in the flux emergence experiments so far (Section 6.2). The final paragraphs point out a number of limitations of the present experiment that may be overcome in the future (Section 6.3).

6.1. Observations

A first block of quantities that can be compared to observations concern the size, timescale and kinematic properties of the surge. A more in-depth comparison must be done through a-posteriori synthesis of different spectral lines based on the numerical boxes. However, the most important spectral lines that one could use for this comparison (like $\text{H}\alpha$, Ca II H+K or $\text{He II } 10830 \text{ \AA}$) require careful treatment including NLTE aspects; this kind of approach must therefore be left for future work.

The height of the surge in our experiment varies considerably in the different stages of the evolution. At the time of maximum development, the ejecta constitute a vertically elongated object with height about 13 Mm and width about 2 Mm. The observed length (see Section 1) falls typically in the interval 10 - 50 Mm, so the height of our surge is within the observed range, even though toward its lower limit. This fits with the fact that the experiment deals with a simple emergence event into a coronal hole, whereas many classical observations refer to surges measured in the context of flare episodes in active regions, which involve a larger amount of magnetic flux and where larger structures should be expected. The cool ejection in our experiment lasts for about 7 - 8 min, which, again, is toward the lower limit of the observed durations (several minutes to one hour, Jiang et al. 2007, Vargas Domínguez et al. 2014). Regarding the velocities, although high velocities of up to 150 km s^{-1} can be reached along the launch phase, during most of the surge evolution the mass elements have rising or falling velocities below 50 km s^{-1} , and the ejection is not collimated. The observations, in turn, yield a velocity range of 10 - 200 km s^{-1} , as inferred mainly from $\text{H}\alpha$ measurements (Roy 1973, Canfield et al. 1996, Chae et al. 1999, Jibben & Canfield 2004, Uddin et al. 2012, Nelson & Doyle 2013, Vargas Domínguez et al. 2014, among others), which is compatible with the results of the experiment.

Concerning the acceleration, in the experiment we have detected two different patterns of behavior: (1) during the launch phase, the mass elements suffer large accelerations, well in excess of solar gravity; (2) when near

the apex of their individual trajectories, the acceleration values are remarkably close to g_{\odot} . There is no definitive observational value to use for a comparison here: in the paper by Roy (1973), the author reports a fast rising phase for the surge with acceleration of $0.24 - 2.1 \text{ km s}^{-2}$, i.e., roughly $1 - 10 g_{\odot}$. Observed values for the acceleration at the time of maximum and in the decay phase are more difficult to obtain. In their recent paper, Nelson & Doyle (2013) detected an apparent parabolic trajectory for the cool ejection in their study, but no particular value for the acceleration was given.

6.2. *The relevance of the entropy sources*

An adequate treatment of the entropy sources and sinks in the energy equation, or, more generally, of the material properties of the plasma, like its EOS, is important when studying the formation and time evolution of the cool ejections. Thanks to the possibilities afforded by the Bifrost code and to an extensive Lagrange tracing of the mass elements of the surge, we have been able to distinguish different patterns of behavior among them and group them into separate populations. One of those populations, Population B, provides a good illustration in that sense. That population covers 34% of the surge cross section at the time of maximum development. It reaches high temperatures, between 10^5 and 10^6 K, typically when going through the current sheet, but is then brought back down to classical surge temperatures of order 10^4 K thanks to the action of the radiation losses and thermal conduction terms. This population could not be obtained in more idealized experiments, like those of Yokoyama & Shibata 1996, Nishizuka et al. 2008, Jiang et al. 2012, Moreno-Insertis & Galsgaard 2013. The first authors, for instance, find that the material in the surge structure is not heated significantly along its life (which would roughly correspond to the behaviour of our populations A and C). Instead, we find that a non-small amount of the plasma in the surge suffers heating/cooling processes that lead them to high temperatures during a fraction of its life. This explains part of the structural properties of the modeled surge and may also be of interest concerning its detection.

The importance of a proper treatment of the entropy sources and of the equation of state may also apply to other cool ejections such as the macrospicules. Chromospheric material and hotter, transition-region material probably coexist in these objects, as indicated by their detection both in $H\alpha$ and in the EUV line He II 304 Å. However, the numerical experiments in the literature (e.g. Murawski et al. 2011; Kayshap et al. 2013) are of the idealized kind, so, while possibly capturing various basic features of the macrospicule phenomenon, they may also miss important aspects.

6.3. *The progress toward realism in the theoretical modeling of surges following from flux emergence*

The essential component in the observed solar surge phenomenon is plasma with chromospheric temperatures and densities, as follows from their detection in spectral lines like $H\alpha$, Ca II H+K, Ca II 8542 Å or He II 10830 Å. Like for other important phenomena of the low solar atmosphere (prominences are a prime example for this), their theoretical study is intricate because of the difficul-

ties of coping with the material properties of the chromospheric plasma. All previous numerical studies of surges following from flux emergence were done on the basis of highly idealized models, without radiation transfer nor a multi-component equation of state with realistic abundances, partial ionization processes, etc. Our present paper constitutes a large step forward in that direction, given the degree of realism of the material modules of the Bifrost code, as explained in Section 2.1. In the following we first compare our results with those of the 3D experiment of Moreno-Insertis & Galsgaard (2013). Then, a few limitations of the present experiment are discussed, namely the presence in flux emergence models of cool and dense plasma domains in the low atmosphere, the effects of partial ionization on Ohm's law and the lack of ionization/recombination equilibrium in processes occurring on short timescales.

Our approach allowed us to gain new insights compared with previous idealized simulations of the ejection of cool surges, even with the recent 3D experiment by Moreno-Insertis & Galsgaard (2013). Major differences between the two experiments come from the inclusion in our case of detailed material properties, radiation transfer and heat conduction, which have allowed us, e.g., to discern different plasma populations that later constitute the cool surge, or to study the initial interaction of the rising plasma with realistic granulation, or to identify the process of detachment and decay of the surge. In a 2D experiment one can reach much higher spatial resolution, which facilitates the study of many aspects difficult or impossible to consider in a 3D problem, like the formation and evolution of plasmoids or the shock structures associated with the jets. Finally, our Lagrange tracing has an extremely high cadence (thanks again to the reduced storage demands of a 2D experiment), and this is advantageous when pursuing the motion of the plasma elements across regions with strong gradients. On the other hand, various general properties of the surge in this paper are in agreement with the simulation of Moreno-Insertis & Galsgaard (2013): being three-dimensional, the cool ejecta in their experiment had the shape of an almost circular plasma wall with chromospheric density surrounding the emerged region, even if the largest concentration was found at the base of the hot jet. There, the cool domain had a height (~ 10 Mm), similar to that obtained in the present 2.5D experiment, and width (~ 6 Mm), which is wider than in the present paper, perhaps because of the lack of realistic convection cells in their experiment, which can modify the horizontal sizes of the emerged structures. The surge velocities, around 50 km s^{-1} , are also within the range given by those authors for their cool ejecta.

When large magnetized plasma domains rise from the solar interior to the low atmosphere, a dense and cold plasma dome is formed, as repeatedly shown in the numerical experiments since the 1990s. At the interface between the dome and the overlying atmospheric material a large density gradient arises. Numerical codes tend to smooth that sharp density contrast through diffusion, in many cases via some explicit diffusion term, like in Bifrost, or, in a less controllable fashion, through the hidden, intrinsic diffusion of the numerical scheme, like in formally ideal MHD codes. Irrespective of whether a process of mixing takes place in such interfaces in the

actual Sun, any result associated with this diffusion in the theoretical models must be handled with care. In our case, we have identified a family of plasma elements originating in coronal heights (population D, Section 4.1.4) whose density is increased to a large extent via this kind of diffusion process when they pass near the current sheet before being incorporated to the surge. The initial mass of this family is negligible compared to the final mass of the surge; in some sense, that family is swallowed by the much more dense material coming from the dome, so the qualitative (and, to a large extent, quantitative) properties of the final surge should be widely independent of the evolution of this particular population. A different issue concerns the dome itself: the large expansion associated with the rise leads it to adopt cold temperatures, below 2000 K. The ad-hoc heating term mentioned in Section 2 is then activated in the calculation to prevent the plasma from cooling to lower temperatures, for which the radiation tables used by Bifrost become inaccurate (see Leenaarts et al. 2011). The material of the surge originates essentially in the dome, so, in spite of the enormous advantages of the new generation of MHD codes compared with the previous idealized models, a fully realistic treatment of the evolution of the surge in its formation stage must await the completion of material modules for the codes adequate to the very cold plasma volumes in the low atmosphere.

In the same vein, another aspect that must be improved in future models of the solar surges is the use of a generalized Ohm's Law incorporating partial ionization effects. On the basis of the general results of Leake & Arber (2006), Arber et al. (2007), Martínez-Sykora et al. (2012, 2015) and Leake & Linton (2013), among others, we expect that these effects may allow some slippage of magnetic field and plasma via ambipolar diffusion and counteract to some extent the cold temperatures of the rising dome. This could affect the populations obtained in the surge, especially Population C, see section 4.1.3. As a final item in the list of limitations in the realism of the current model, we mention

here the lack of non-thermal equilibrium in the ionization/recombination processes of hydrogen and helium. As already proposed long ago (Kneer 1980), in chromospheric processes that occur on comparatively fast time scales (e.g., in shocks), the ionized species, especially hydrogen and helium, may take longer to recombine than predicted by local-thermodynamic-equilibrium (LTE) equations (see the recent results by Leenaarts et al. 2007 and Golding et al. 2014). This problem is particularly important if one tries to obtain a posteriori, i.e., on the basis of the calculated computational boxes, synthetic spectra for the hydrogen or helium lines from plasma at temperatures around 6×10^3 K (for H) or between 1 and 2×10^4 K (for He). However, the time evolution of the system itself may also be affected in a non-negligible way by this departure of LTE. The inclusion of the non-equilibrium effects into the models of surges is therefore another improvement that must be incorporated in future extensions of the present work.

We gratefully acknowledge financial support by the Spanish Ministry of Economy and Competitiveness (MINECO) through projects AYA2011-24808 and AYA2014-55078-P, as well as by NASA through grants NNX11AN98G, NNM12AB40P and NNX14AI14G (HGCR grant) and contracts NNM07AA01C (Hinode) and NNG09FA40C (IRIS). The authors thankfully acknowledge the computer resources and the technical expertise and assistance provided at the LaPalma supercomputer installation (IAC, Spain) and at the Teide High-Performance Computing facilities (Instituto Tecnológico y de Energías Renovables, ITER, Spain), where the calculations presented in this paper were carried out. Use for test runs of the Pleiades cluster through the computing project s1061 from NASA's HEC division is also acknowledged. Finally, the authors are grateful to the members of the Bifrost development team for their help with the Bifrost code, and to the anonymous referee for his/her constructive comments.

REFERENCES

- Arber, T. D., Haynes, M., & Leake, J. E. 2007, *ApJ*, 666, 541
 Archontis, A., Moreno-Insertis, F., Galsgaard, K., Hood, A., & O'Shea, E. 2004, *A&A*, 426, 1047
 Archontis, V., Galsgaard, K., Moreno-Insertis, F., & Hood, A. W. 2006, *ApJ*, 645, L161
 Archontis, V., & Hansteen, V. 2014, *ApJ*, 788, L2
 Bennett, S. M., & Erdélyi, R. 2015, *ApJ*, 808, 135
 Bohlin, J. D., Vogel, S. N., Purcell, J. D., Sheeley, Jr., N. R., Tousey, R., & Vanhoosier, M. E. 1975, *ApJ*, 197, L133
 Brooks, D. H., Kurokawa, H., & Berger, T. E. 2007, *ApJ*, 656, 1197
 Canfield, R. C., Reardon, K. P., Leka, K. D., Shibata, K., Yokoyama, T., & Shimojo, M. 1996, in *IAU Colloq. 153: Magnetodynamic Phenomena in the Solar Atmosphere - Prototypes of Stellar Magnetic Activity*, ed. Y. Uchida, T. Kosugi, & H. S. Hudson, 49
 Cao, T.-j., Xu, A.-a., & Tang, Y.-h. 1980, *Chinese Astronomy*, 4, 143
 Carlsson, M., & Leenaarts, J. 2012, *A&A*, 539, A39
 Chae, J., Qiu, J., Wang, H., & Goode, P. R. 1999, in *Bulletin of the American Astronomical Society*, Vol. 31, American Astronomical Society Meeting Abstracts #194, 963
 Cheung, M. C. M., Schüssler, M., & Moreno-Insertis, F. 2007, *A&A*, 467, 703
 Ellison, M. A. 1942, *MNRAS*, 102, 22
 Fan, Y. 2001, *ApJ*, 554, L111
 Finn, J. M., & Kaw, P. K. 1977, *Physics of Fluids*, 20, 72
 Forbes, T. G., & Priest, E. R. 1984, *Sol. Phys.*, 94, 315
 Furth, H. P., Killeen, J., & Rosenbluth, M. N. 1963, *Physics of Fluids*, 6, 459
 Golding, T. P., Carlsson, M., & Leenaarts, J. 2014, *ApJ*, 784, 30
 Goldston, T. P., & Rutherford, P. H. 1995, *Introduction to Plasma Physics* (CRC Press)
 Gudiksen, B. V., Carlsson, M., Hansteen, V. H., Hayek, W., Leenaarts, J., & Martínez-Sykora, J. 2011, *A&A*, 531, A154+
 Gudiksen, B. V., & Nordlund, Å. 2005, *ApJ*, 618, 1020
 Guglielmino, S. L., Bellot Rubio, L. R., Zuccarello, F., Aulanier, G., Vargas Domínguez, S., & Kamio, S. 2010, *ApJ*, 724, 1083
 Habbal, S. R., & Gonzalez, R. D. 1991, *ApJ*, 376, L25
 Hansteen, V. H., Carlsson, M., & Gudiksen, B. 2007, in *Astronomical Society of the Pacific Conference Series*, Vol. 368, *The Physics of Chromospheric Plasmas*, ed. P. Heinzel, I. Dorotović, & R. J. Rutten, 107
 Hansteen, V. H., De Pontieu, B., Rouppe van der Voort, L., van Noort, M., & Carlsson, M. 2006, *ApJ*, 647, L73
 Hayek, W., Asplund, M., Carlsson, M., Trampedach, R., Collet, R., Gudiksen, B. V., Hansteen, V. H., & Leenaarts, J. 2010, *A&A*, 517, A49+
 Heyvaerts, J., Priest, E. R., & Rust, D. M. 1977, *ApJ*, 216, 123
 Jiang, R.-L., Fang, C., & Chen, P.-F. 2012, *ApJ*, 751, 152
 Jiang, Y. C., Chen, H. D., Li, K. J., Shen, Y. D., & Yang, L. H. 2007, *A&A*, 469, 331
 Jibben, P., & Canfield, R. C. 2004, *ApJ*, 610, 1129
 Kayshap, P., Srivastava, A. K., Murawski, K., & Tripathi, D. 2013, *ApJ*, 770, L3
 Kirshner, R. P., & Noyes, R. W. 1971, *Sol. Phys.*, 20, 428
 Kneer, F. 1980, *A&A*, 87, 229

- Kurokawa, H., & Kawai, G. 1993, in *Astronomical Society of the Pacific Conference Series*, Vol. 46, IAU Colloq. 141: The Magnetic and Velocity Fields of Solar Active Regions, ed. H. Zirin, G. Ai, & H. Wang, 507
- Leake, J. E., & Arber, T. D. 2006, *A&A*, 450, 805
- Leake, J. E., & Linton, M. G. 2013, *ApJ*, 764, 54
- Leenaarts, J., Carlsson, M., Hansteen, V., & Gudiksen, B. V. 2011, *A&A*, 530, A124
- Leenaarts, J., Carlsson, M., Hansteen, V., & Rutten, R. J. 2007, *A&A*, 473, 625
- Madjarska, M. S., Doyle, J. G., Hochedez, J.-F., & Theissen, A. 2006, *A&A*, 452, L11
- Magara, T. 2001, *ApJ*, 549, 608
- Martínez-Sykora, J., De Pontieu, B., & Hansteen, V. 2012, *ApJ*, 753, 161
- Martínez-Sykora, J., De Pontieu, B., Hansteen, V., & Carlsson, M. 2015, *Royal Society of London Philosophical Transactions Series A*, 373, 40268
- Martínez-Sykora, J., Hansteen, V., & Carlsson, M. 2008, *ApJ*, 679, 871
- Moreno-Insertis, F. 2006, in *Solar MHD Theory and Observations: A High Spatial Resolution Perspective ASP Conference Series*, Vol. 354, 183
- Moreno-Insertis, F., & Galsgaard, K. 2013, *ApJ*, 771, 20
- Moreno-Insertis, F., Galsgaard, K., & Ugarte-Urra, I. 2008, *ApJ*, 673, L211
- Murawski, K., Srivastava, A. K., & Zaqarashvili, T. V. 2011, *A&A*, 535, A58
- Murray, M. J., Hood, A. W., Moreno-Insertis, F., Galsgaard, K., & Archontis, V. 2006, *A&A*, 460, 909
- Nelson, C. J., & Doyle, J. G. 2013, *A&A*, 560, A31
- Newcomb, W. A. 1961, *Physics of Fluids*, 4, 391
- Newton, H. W. 1942, *MNRAS*, 102, 2
- Nishizuka, N., Shimizu, M., Nakamura, T., Otsuji, K., Okamoto, T. J., Katsukawa, Y., & Shibata, K. 2008, *ApJ*, 683, L83
- Orozco Suárez, D., Bellot Rubio, L. R., del Toro Iniesta, J. C., & Tsuneta, S. 2008, *A&A*, 481, L33
- Ortiz, A., Bellot Rubio, L. R., Hansteen, V. H., de la Cruz Rodríguez, J., & Rouppe van der Voort, L. 2014, *ApJ*, 781, 126
- Pike, C. D., & Harrison, R. A. 1997, *Sol. Phys.*, 175, 457
- Roy, J.-R. 1973, *Sol. Phys.*, 32, 139
- Rust, D. M. 1976, *Philosophical Transactions of the Royal Society of London Series A*, 281, 353
- Schlüter, A. 1957, in *Radio astronomy, Proceedings from 4th IAU Symposium*, Vol. 4, 356
- Schmahl, E. J. 1981, *Sol. Phys.*, 69, 135
- Schmieder, B., Mein, P., Martres, M. J., & Tandberg-Hanssen, E. 1984, *Sol. Phys.*, 94, 133
- Schmieder, B., Shibata, K., van Driel-Gesztelyi, L., & Freeland, S. 1995, *Sol. Phys.*, 156, 245
- Shibata, K., Nozawa, S., & Matsumoto, R. 1992, *PASJ*, 44, 265
- Skartlien, R. 2000, *ApJ*, 536, 465
- Stein, R. F., & Nordlund, Å. 1998, *ApJ*, 499, 914
- Tortosa-Andreu, A., & Moreno-Insertis, F. 2009, *A&A*, 507, 949
- Uddin, W., Schmieder, B., Chandra, R., Srivastava, A. K., Kumar, P., & Bisht, S. 2012, *ApJ*, 752, 70
- Vargas Domínguez, S., Kosovichev, A., & Yurchyshyn, V. 2014, *ApJ*, 794, 140
- Yang, L., He, J., Peter, H., Tu, C., Zhang, L., Feng, X., & Zhang, S. 2013, *ApJ*, 777, 16
- Yokoyama, T., & Shibata, K. 1995, *Nature*, 375, 42
- . 1996, *PASJ*, 48, 353
- Yoshimura, K., Kurokawa, H., Shimojo, M., & Shine, R. 2003, *PASJ*, 55, 313
- Zwaan, C. 1987, *ARA&A*, 25, 83